

Connor G. Mulcahy

Department of Mechanical Engineering,
Massachusetts Institute of Technology,
Cambridge, MA 02139

Tianxiang Su

Schlumberger-Doll Research Center,
Cambridge, MA 02139

Nathan Wicks

Schlumberger-Doll Research Center,
Cambridge, MA 02139

Pedro M. Reis

Department of Civil and
Environmental Engineering,
Department of Mechanical Engineering,
Massachusetts Institute of Technology,
Cambridge, MA 02139

Extending the Reach of a Rod Injected Into a Cylinder Through Axial Rotation

We investigate continuous axial rotation as a mechanism for extending the reach of an elastic rod injected into a horizontal cylindrical constraint, prior to the onset of helical buckling. Our approach focuses on the development of precision desktop experiments to allow for a systematic investigation of three parameters that affect helical buckling: rod rotation speed, rod injection speed, and cylindrical constraint diameter. Within the parameter region explored, we found that the presence of axial rotation increases horizontal reach by as much as a factor of 5, when compared to the nonrotating case. In addition, we develop an experimentally validated theory that takes into account anisotropic friction and torsional effects. Our theoretical predictions are found to be in good agreement with experiments, and our results demonstrate the benefits of using axial rotation for extending reach of a rod injected into a constraining pipe.

[DOI: 10.1115/1.4032500]

1 Introduction

Buckling of a slender rod within a cylindrical constraint is observed across a variety of systems and length scales, including vascular catheters [1], silicon nanorods confined within a channel [2], and plant roots penetrating into soil [3]. At the kilometer scale, coiled tubing is commonly used in the oil and gas industries for cleaning, damage repair, and monitoring operations for servicing previously drilled wellbores [4,5]. In the horizontal sections of these wellbores, axial forces build up due to gravity-induced friction between the coiled tubing and the inner surface of the wellbore [6]. These compressive forces increase as the length of injected tubing increases, eventually resulting in buckling and subsequent lockup, thereby preventing further reach into the wellbore [7]. This phenomenon bars coiled tubing from accessing the entire length of modern horizontal wellbores, which can be as long as 11 km (Refs. [8,9]).

A number of previous investigations have examined the buckling conditions for a cylindrically constrained rod. A common and widely studied configuration focuses on idealized boundary conditions by considering a fixed length of rod under axial compression [10–18]. Closer to coiled tubing operations, McCourt et al. [19] and Wicks et al. [20] have studied the case of progressively injecting a rod into a horizontal constraint. Developing strategies to delay the onset of buckling is of particular engineering relevance, in order to accomplish greater injection lengths and thereby increase reach into the wellbore. One avenue to achieve this extended reach is to optimize the control parameters of the system, including increasing the pipe diameter [21] or reducing friction between the coiled tubing and wellbore using lubricants [22]. Mechanical methods have also been considered, including tractors [23] or vibration of the coiled tubing [24,25]. An alternative strategy is to use axial rotation, which has been proposed in field scale studies as a mechanism to reduce axial forces induced by friction during coiled tubing operations [24,26]. Still, there is a timely need to develop predictive theoretical frameworks that rationalize the effects of axial rotation on constrained buckling in coiled tubing operations, and that are accurately and systematically validated by precision experiments.

Here, we present a combined experimental and theoretical investigation on the extension of reach of a slender rod injected into a cylindrical constraint by the introduction of axial rotation.

Contributed by the Applied Mechanics Division of ASME for publication in the JOURNAL OF APPLIED MECHANICS. Manuscript received December 16, 2015; final manuscript received January 12, 2016; published online February 19, 2016. Editor: Yonggang Huang.

Continuous rotation at the injection end leads to an overall reduction of the axial forces due to friction, thereby delaying the onset of buckling. By exploring the parameter space of the problem, we demonstrate that the injection reach can be increased by as much as a factor of 5, when compared to the case of injection without rotation. A theoretical analysis of the problem has enabled us to rationalize the underlying mechanics and predict the overall behavior. We show that reach extension depends directly on the ratio between the injection and rotation speeds of the rods. In our experimental system, we also find that anisotropic friction is important. Although implementation of axial rotation is a difficult engineering challenge, these findings demonstrate the potential of this strategy to achieve a substantial extension of reach in coiled tubing operations in horizontal wellbores.

Our paper is organized as follows: In Sec. 2, we provide a definition of the problem. The desktop-scaled apparatus and the experimental protocol used to simultaneously rotate and inject a rod into a cylindrical constraint are presented in Sec. 3. In Sec. 4, we describe the experimental results on reach extension and a theoretical analysis for the problem is performed in Sec. 5. In Sec. 6, we return to the experiments for testing and validation of some of the primary assumptions of the theory. We finish with a direct comparison between theory and experiments in Sec. 7 and with some concluding remarks in Sec. 8.

2 Definition of the Problem

A schematic diagram of our problem is presented in Fig. 1. A thin elastic rod of radius R is progressively injected at speed v into a horizontal cylindrical constraining pipe of diameter D , with the possibility of also simultaneously rotating it axially at angular speed ω . The position along the rod is described by the arc-length s of its centerline with $s = 0$ at the free tip and $s = l$ at the injection point, where l is the total length of rod injected into the cylinder. The rod is initially straight and lies on the bottom of the cylinder. During injection, axial forces arise due to friction from the progressive increase in the extent of contact between the rod and the constraint. These axial forces are compressive with a linear spatial profile from zero at the free tip up to a maximum value at the injection point. When the axial force reaches critical values, a series of buckling instabilities occurs that causes the originally straight rod to lose stability and geometrically nonlinear configurations emerge.

The buckling modes are initiated near the injection site, where the axial stresses are highest, such that the buckled configuration of the rod is spatially heterogeneous. The first buckling mode

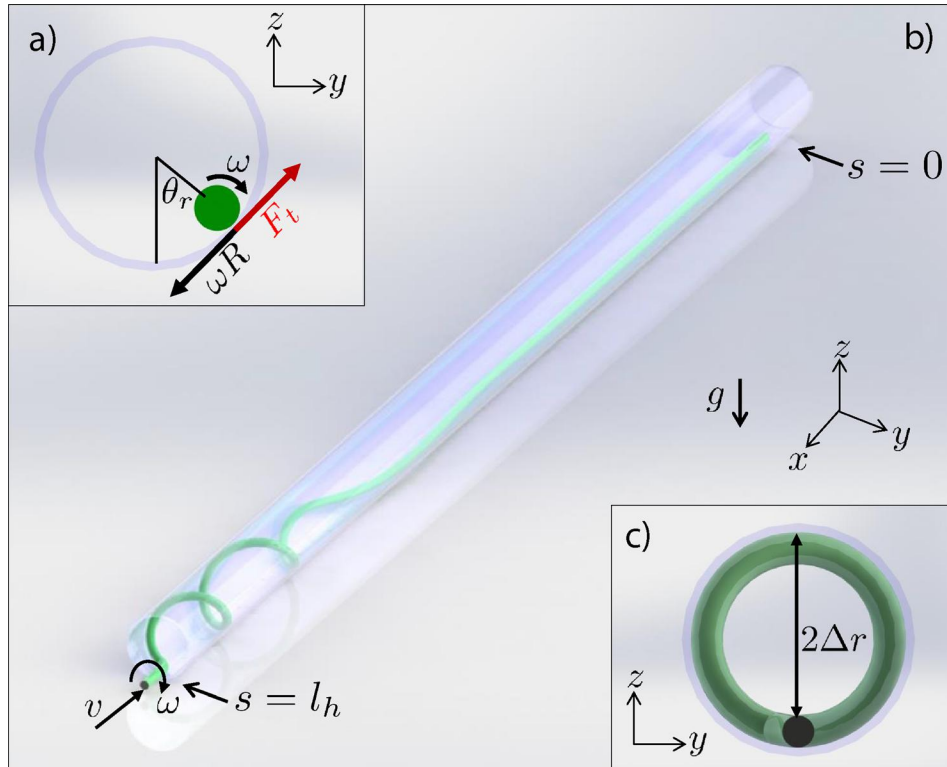


Fig. 1 Schematic definition of the problem. (a) Diagram of transverse forces exerted on the rod during axial rotation. (b) Representation of the helical buckling configuration that occurs when the injected length of the rod is l_h . (c) Definition of the radial clearance, Δr , between the rod and the constraint.

consists of a sinusoidal configuration near the injection site, connected to a straight portion until the tip of the rod. Upon subsequent injection, a secondary instability occurs; the rod buckles into a mode consisting of a helical configuration near the injector, an intermediate sinusoidal region, and a straight portion until the free tip. Once the helix forms, there is a sharp increase in the contact forces near the injector that causes the rod to jam [27]. At this point, no further reach into the constraint is possible, which is analogous to the *lockup* in the coiled tubing operations [28] mentioned in the introduction.

To describe the onset of this jamming process, we focus on quantifying the *helical buckling length*, which is the length of injected rod at which the helices first form. As we shall show, this helical buckling length can be increased significantly by axially rotating the rod during injection. For the base case *without* rotation, we refer to this quantity as $l_h^0 = \hat{l}_h(\omega = 0)$, and for the case *with* rotation as $l_h = \hat{l}_h(\omega > 0)$. Our main quantity of interest to assess the conditions that lead to extension of horizontal reach into the constraint is the normalized helical buckling length, $\bar{l}_h = l_h/l_h^0$. In Sec. 4, we will show that the primary control parameter for the system is the dimensionless ratio, $\alpha = \omega R/v$, of the velocities at the surface of the rod due to rotation and injection.

For the nonrotating case, McCourt et al. [19] and Wicks et al. [20] have developed a prediction for the length of rod injected at the onset of helical buckling

$$l_h^0 = \frac{2\sqrt{2}}{\mu} \sqrt{\frac{EI}{w\Delta r}} \quad (1)$$

where μ is the coefficient of friction between the rod and the constraint; E , I , and w are the elastic modulus, areal moment of inertia, and weight per unit length of the rod, respectively; and Δr is the radial clearance between the rod and the constraint (see Fig. 1(c)). This prediction has since been validated by Miller et al.

[25] through systematic precision desktop experiments. The main goal of our current study is to extend the understanding of this buckling phenomenon to include the case of an axially rotating rod. In particular, we seek to describe, rationalize, and develop a predictive framework for the dependence of \bar{l}_h on α that encodes the conditions that can lead to the extension of horizontal reach of a rod injected into a cylindrical constraint.

3 Experimental Apparatus and Protocol

In Fig. 2(a), we present a photograph of the apparatus that we used to study the problem defined above. As in our previous work [18,25,27], we chose to perform precision experiments in the laboratory, at the desktop-scale. The advantages of this approach compared to field studies of coiled tubing operations at the kilometer scale include rapid exploration of a large range of experimental parameters, direct measurement of geometric and material properties that are difficult to obtain in the field, and well-defined boundary conditions. Miller et al. [27] performed a formal scaling analysis that established the validity of this methodology by showing that the behavior observed in the laboratory can be translated directly onto the field scale by making use of the appropriate dimensionless parameters.

Similarly to the experiments conducted by Miller et al. [25,27], a thin elastomeric rod (more details below) was injected into a cylindrical constraining pipe made of borosilicate tubing with diameters in the range $12 \leq D$ (mm) ≤ 34 and length $L = 4.84$ m. A particularly novel and technically challenging feature of the new apparatus of the current study is the need to continuously rotate the rod at the same time that it is being injected into the pipe. In Fig. 2(b), we present a rendering of the rotary injection system positioned at one of the extremities of the pipe. Figure 2(c) shows a detail of the actual injection unit, which was aligned with the bottom surface of the pipe.

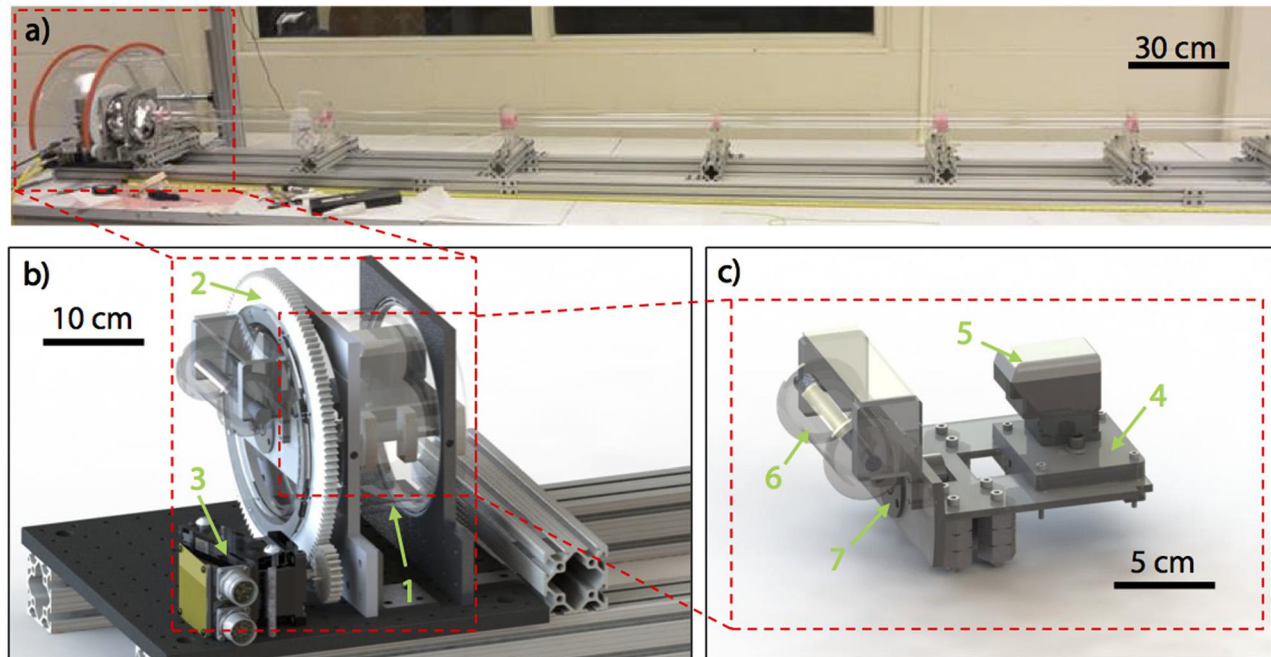


Fig. 2 (a) Photograph of the apparatus used to simultaneously rotate and inject a thin elastomeric rod into a borosilicate pipe laid horizontally. (b) Rendering of the rotary injection assembly. A cylindrical PMMA housing (1) is mounted on two rotary bearings (2) connected to a servomotor (3). (c) Rendering of the injection unit mounted within the rotating housing. The injector head (4) is driven by a stepper motor (5). To prevent twisting, the rod is stored on a spool (6) and the electronics are connected externally by a rotary slip ring (7).

The rod was rotated axially by mounting the injection unit inside a rotating polymethyl methacrylate (PMMA) housing (see Fig. 2(b)). The housing was itself rotated through a geared transmission connected to a DC servomotor (Parker Motion BE230F DC motor), which enabled rotation speeds in the range $0 \leq \omega$ (rpm) ≤ 300 monitored by an onboard encoder. Simultaneously to and independently of the rotation, the rod was injected into the pipe by a pinch-wheel style injector head (see Fig. 2(c)) controlled using a stepper motor (Intelligent Motor Systems MDrive 14 Plus Motion Control). The explored range of injection speed was $0 \leq v$ (cm/s) ≤ 1 . Due to the rotary nature of the apparatus, special care was taken to prevent twisting of the various components; the rod was stored on a spool mounted directly onto the injector and all electrical connections were routed through a rotary slip ring connection.

The rods used in these experiments were fabricated in house using the same protocol developed by Miller et al. [25,27]. In summary, a two-part vinyl polysiloxane polymer (VPS, Zhermack Elite Double 32) was cast inside a set length of polyvinyl chloride tubing. During curing, the tubing was kept straight to produce rods with no natural curvature along their lengths. The rods produced using this method had a constant radius of $R = 1.58 \pm 0.03$ mm and lengths of up to $l_R = 6$ m. The density of these rods was measured to be $\rho = 1210 \pm 8$ kg/m², the Young's modulus was $E = 1290 \pm 12$ kPa, and the Poisson ratio was $\nu \approx 0.5$. Prior to an experimental test, the rod was preconditioned by coating it with chalk (Irwin Strait-Line marking chalk) to create a constant axial frictional coefficient of $\mu_a = 0.54 \pm 0.05$ between the rod and the cylindrical constraint. This value of μ_a was previously measured by Miller et al. by applying a linear fit to the force required to inject the rod into the constraint prior to buckling [25].

We proceed by describing the experimental protocol followed to systematically measure the helical buckling length, l_h , for different experimental conditions. First, the rod was injected into the pipe at constant speed, v , and rotational speed, ω . The injection was halted at the moment of onset of helical buckling (defined by the moment when the first formed helix becomes in contact with the top surface of the pipe). The process was imaged by a digital

camcorder (Logitech HD Pro Webcam C920, 30 fps) positioned above the injection site. Image analysis of the recorded videos allowed us to determine the time interval, Δt , between the start of injection and the onset of helical buckling. Using the known injection speed, the helical buckling length was then readily determined as $l_h = v\Delta t$.

A series of experiments was conducted to explore the parameter space of the system by varying the following quantities: three values of the constraint diameters in the range $12.1 \leq D$ (mm) ≤ 34 , three values of the injection speed in the range $0.25 \leq v$ (cm/s) ≤ 1 , and axial rotation speeds in the range $0 \leq \omega$ (rpm) ≤ 300 . Throughout, the mechanical properties of the rod (elastic modulus, density, friction coefficient) were kept fixed. For each set of parameters, five identical experimental runs were conducted, and each reported experimental data point corresponds to the average of these measurements and its error bar to the standard deviation. To ensure reproducibility, prior to each group of five runs, the pipe was cleaned with ethanol to remove residual impurities and chalk was reapplied to the rod to ensure constant and reproducible frictional conditions across all experiments.

4 Experimental Results, Part I: Extension of Reach

We now present the results of a series of experiments that made use of the apparatus and protocol described in Sec. 3. In Fig. 3, we plot the normalized helical buckling length, \bar{l}_h , as a function of the dimensionless rotation speed, α , for three different values of the injection speed, $v = \{0.25, 0.5, 1\}$ cm/s, and constraint diameters, $D = \{12.0, 21.7, 34.0\}$ mm. For each of these constraint diameters, the nonrotating ($\omega = 0$ rpm) buckling length, l_h^0 , was first measured using the procedure outlined above, yielding $l_h^0 = \{0.90 \pm 0.07, 0.73 \pm 0.04, 0.62 \pm 0.03\}$ m, respectively.

The results show that \bar{l}_h increases monotonically and sublinearly with α . The data for different injection speeds and pipe diameters collapse into a master curve, which further support the appropriateness of the dimensionless parameter α . Moreover, the data suggest that the radial clearance has little effect on the behavior and, if any, it is within the experimental uncertainty of the

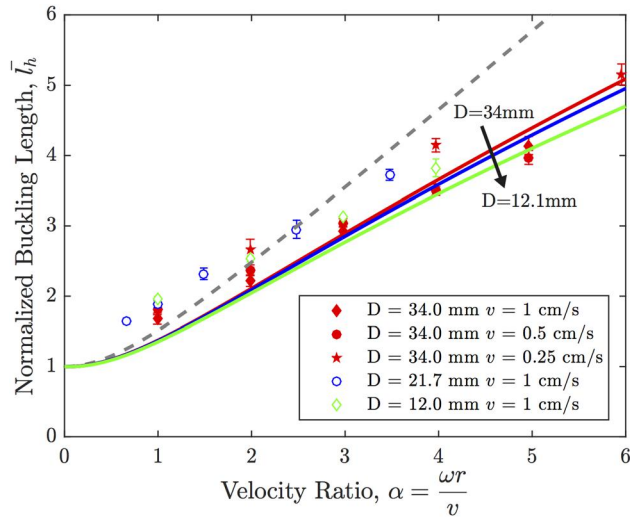


Fig. 3 Normalized buckling length, \bar{l}_h versus dimensionless rotation speed, α . The experiments were conducted in the following ranges of parameters: $12.1 \leq D$ (mm) ≤ 34 ; $0.25 \leq v$ (cm/s) ≤ 1 ; and $0 \leq \omega$ (rpm) ≤ 300 . The dashed line represents the simplified theory given by Eq. (7), and the solid lines represent the more sophisticated theory given by Eq. (18).

measurements. When compared to the nonrotating case ($\alpha = 0$), the horizontal reach of the rod can be extended by a factor as large as 5.1 for $\alpha = 5.96$. This value is particularly significant in the context of coiled tubing operations because it suggests that axial rotation has the potential to offer reach extension well beyond current methods.

5 Theoretical Analysis

We proceed by developing a predictive theoretical framework for the buckling length of an axially rotating rod injected into a constraint. The analysis is based on scaling arguments [27] such that the predictions should apply to both the kilometer-scale coiled tubing operations introduced in Sec. 1, as well as the meter-scale desktop experiments described throughout this paper.

5.1 Assumptions. Our analysis has a number of assumptions listed next, which will eventually be validated against experiments in Sec. 6. *Assumption 1:* The rise of the rod due to rotation is uniform from the injection end to the free tip. Due to the friction in the transverse direction, the rotating rod rises up the side of the constraining pipe from its bottom position (see schematic in the inset of Fig. 1). However, note that in our experiments, the point of injection is fixed at the bottom of the cylinder, such that the rise of the rod is not uniform throughout the entirety of its arc-length. For simplicity of the analysis, we neglect this effect and assume that the rod rises uniformly up to an angle that is dictated by the friction in the transverse direction. *Assumption 2:* The normal contact force between the rod and the cylinder constraint is uniform along the rod. *Assumption 3:* Friction is anisotropic and can be modeled by a two-dimensional friction coefficient tensor whose two principle directions are the axial and transverse directions of the rod.

5.2 Frictional Contact Between the Rod and Constraint: Effect of Rotation. Given the simultaneous injection and rotation, there are two nonzero components for both the contact point velocity and the friction force vectors: an axial component due to the injection and a transverse component due to the axial rotation. In the nonrotating case, the axial component of friction dominates the behavior. To compute the friction force in the axial and

transverse directions (denoted by \hat{a} and \hat{t} , respectively), we consider anisotropic friction such that the friction coefficient tensor is

$$\boldsymbol{\mu} = \mu_a \hat{a} \otimes \hat{a} + \mu_t \hat{t} \otimes \hat{t} \quad (2)$$

where μ_a and μ_t are the friction coefficients in the two principal directions. Using this friction coefficient tensor, the Coulomb friction force can be computed as

$$\mathbf{f} = -(\boldsymbol{\mu} \cdot \hat{v})N = -\frac{\mu_a N}{\sqrt{1 + \alpha^2}} \hat{a} - \frac{\mu_t \alpha N}{\sqrt{1 + \alpha^2}} \hat{t} \quad (3)$$

where N is the normal contact force per unit reference length of the rod, \hat{v} is the unit (normalized) vector of the contact point velocity, and the dimensionless velocity ratio (assumed to be constant along the entire length of the rod) is

$$\alpha = \frac{\omega R}{v} \quad (4)$$

Since the rod does not rest at the bottom of the constraining cylinder due to the rotation, in Eq. (3), the magnitude of the normal contact force per unit length, N , is smaller than the gravitational load acting on the rod. As such, the rod climbs up the inner surface of the cylinder due to the transverse friction force (see Fig. 1(a)), which partly balances the gravitational load so that N is reduced. Assuming quasi-static conditions, a force balance analysis yields an expression for N as a function of the transverse friction coefficient μ_t and velocity ratio α

$$N(\alpha) = \frac{\rho g A}{\sqrt{1 + \mu_t^2 \alpha^2 / (1 + \alpha^2)}} \quad (5)$$

where $\rho g A$ is the gravitational load acting on a unit length of the rod of cross-sectional area, A .

The components of the friction force in both the axial (\hat{a}) and transverse (\hat{t}) directions can now be obtained by plugging the expression of the normal contact force, Eq. (5), into Eq. (3). In particular, the friction force in the axial direction, $f_a = \mathbf{f} \cdot \hat{a}$, can be used to compute the compression along the rod

$$F_a(s) = \int_0^s f_a ds = \frac{\mu_a \rho g A s}{\sqrt{1 + (1 + \mu_t^2) \alpha^2}} \quad (6)$$

where s is the reference arc-length ($s = 0$ at the free end, and $s = l$ at the injection end). As expected, due to friction, the axial compression along the rod increases linearly with s , reaching a maximum at $s = l$. This description is valid only while the configuration of the rod is straight, i.e., prior to the first buckling instability into the sinusoidal mode. However, we assume that this continues to be valid up to the onset of helical buckling. We assume that buckling occurs when the maximum compression reaches a critical buckling force, $F_a(l_h) = F_{cr}$, which leads to the following prediction for the critical buckling length:

$$l_h = \sqrt{1 + (1 + \mu_t^2) \alpha^2} \frac{F_{cr}}{\mu_a \rho g A} \quad (7)$$

5.3 The Critical Buckling Force, F_{cr} . There are two buckling modes (sinusoidal and helical) for a confined rod under compression. Previously, it has been shown that sinusoidal buckling (where the rod snakes along the bottom of the cylinder) is benign because the normal contact force and the axial friction force do not increase significantly past this first instability [27]. By contrast, helical buckling leads to a rapid increase of these forces and causes lockup of the rod [27]. Therefore, the helical mode is one

of the primary importances in determining lockup and we shall focus of our attention on its onset.

In the absence of rotation, the following prediction for the critical helical buckling load is commonly used in the oil and gas industry [13]

$$F_{cr}^0 = 2\sqrt{2} \sqrt{\frac{EIw}{\Delta r}} \quad (8)$$

where EI is the bending stiffness of the rod, $w = \rho gA$ is the weight per unit length, and Δr is the radial clearance. Previous studies [26] have attempted to estimate the effect of rotation on the reduction of friction, and consequently on lockup, by making use of Eq. (8). However, we argue that this framework needs to be appropriately modified when introducing rotation, for the two important reasons detailed next.

(i) There is a combined bending and gravitational energetic cost for a rod to buckle into a helical configuration. Let us focus on the gravitational contribution. Without rotation, for buckling to occur, the originally straight rod needs to be lifted into a helical configuration whose center of mass is a distance Δr above the bottom of the cylinder. However, if the rod is simultaneously rotated during injection, prior to buckling, the straight configuration of the rod has already been raised by an angle θ_r (see inset of Fig. 1). As such, the gravitational cost is reduced when compared with the nonrotating case and we expect a smaller critical buckling force than that predicted by Eq. (8). Quantitatively, for the case with rotation, the gravitational energy cost, per unit rod length, from a lifted straight configuration to a helical configuration is

$$\Delta \mathcal{E} = \rho gA \Delta r \cos \theta_r \quad (9)$$

where the equilibrium rise angle

$$\theta_r = a \cos \left(\frac{1}{\sqrt{1 + \mu_t^2 \alpha^2 / (1 + \alpha^2)}} \right) \quad (10)$$

is derived from a force balance analysis assuming quasi-static conditions. The critical buckling force, F_{cr} , can be obtained by balancing the potential of the compressive force with the increase of the sum of bending and gravitational energies, as outlined by Chen et al. [13]. Following this same procedure and using Eq. (9) as the change of gravitational energy, we can obtain a modified critical buckling force, which is identical to Eq. (8), but with $w = N(\alpha)$ given by Eq. (5), instead of $w = \rho gA$ for the nonrotating case.

(ii) Whereas the axial component of the friction induces compression along the rod, its transverse component induces twisting. In particular, the higher the rotational speed (or the dimensionless velocities ratio, α), the larger the friction in the transverse direction, and, consequently, the greater is the extent of twist along the rod. It is well known that a twisted rod will buckle at a lower magnitude of compressive load [28]. To take the effect of twisting into account, we modulate the critical buckling force by a dimensionless twisting factor $k(\alpha) \leq 1$

$$F_{cr}(\alpha) = 2\sqrt{2} k(\alpha) \sqrt{\frac{EIN(\alpha)}{\Delta r}} \quad (11)$$

This expression, with $k(0) = 1$, reduces to Eq. (8) in the absence of rotation ($\alpha = 0$).

5.4 Extension of the Helical Buckling Length by Rotation. When $\alpha > 0$, the predicted helical buckling length can now be readily obtained by plugging Eqs. (11) and (5) into Eq. (7). We choose to quantify the extension of reach due to rotation by the normalized buckling length, $\bar{l}_h = l_h/l_h^0$, where l_h and l_h^0 are the buckling lengths corresponding to the rotating and nonrotating cases (through Eq. (1)), respectively

$$\bar{l}_h = k(\alpha) ([1 + \alpha^2][1 + (1 + \mu_t^2)\alpha^2])^{1/4} \quad (12)$$

$k(\alpha)$, in Eq. (12) is yet to be determined. For this purpose, we make use of the results of a confined rod under uniform compression and torsion and assume that the obtained critical buckling load is applicable to our case with progressive injection. This assumption is motivated by the fact that a similar approach has been successfully applied in previous studies for the case without rotation [13,29].

With the goal of determining $k(\alpha)$, let us start by considering the force equilibrium of a pure helix confined in a cylindrical channel under end-to-end applied force, F , and twisting torque, T [30]

$$\frac{8\pi^4 EI}{P^4} = \frac{2\pi^2 F}{P^2} + \frac{4\pi^3 T}{P^3} - \frac{\rho gA}{\Delta r} \quad (13)$$

where P is the helical pitch. This equation can be nondimensionalized as

$$f = \frac{1}{2p^2} + \frac{p^2}{2} - \frac{t}{\sqrt{2}p} \quad (14)$$

where $f = F/F_{cr}^0$ is the axial force normalized by the critical buckling force in the absence of rotation, F_{cr}^0 (see Eq. (8)), $p = P/\lambda_s$ is the helical pitch made dimensionless by the sinusoidal buckling wavelength (for the nonrotation case) $\lambda_s = 2\pi(EI\Delta r/\rho gA)^{1/4}$ [31], and $t = T/\sqrt{F_{cr}^0 EI}$ is the dimensionless torque. For a given applied torque, t , there is a critical applied force, f_{cr} , beyond which a real solution for p exists. Helical buckling occurs when $f \geq f_{cr}$ (below this threshold there are no helical configurations that satisfy force equilibrium). Solving $df/dp = 0$ at a fixed value of t yields

$$f_{cr} = \frac{\sqrt{2}}{\sqrt{t^2 + 8} - t} + \frac{\sqrt{t^2 + 8} - t}{4\sqrt{2}} - t \sqrt{\frac{\sqrt{2}}{\sqrt{t^2 + 8} - t}} \quad (15)$$

We note that, above, we defined $f_{cr} = F_{cr}/F_{cr}^0$ as the reduction factor of the critical buckling force due to rotation, and revisiting Eq. (11), we now recognize that $k(\alpha) = f_{cr}$.

The final step is to obtain the actual expression for $k(\alpha)$. We recall from Eq. (6) that, prior to buckling, the internal force (induced by axial friction) of a rod that is simultaneously injected and rotated increases linearly as a function of arc-length, s . A similar argument can be constructed to state linearity of the internal torque (induced by transverse friction) along s . In a dimensionless form, their ratio is

$$\frac{t}{f} = 128^{1/4} \pi \alpha \bar{\mu} \frac{R}{\lambda_s} \quad (16)$$

where $\bar{\mu} = \mu_t/\mu_a$, and λ_s is the sinusoidal critical buckling wavelength mentioned earlier. In general, Eqs. (15) and (16) must be solved numerically to eliminate t , and obtain a solution for $f_{cr}(\alpha) = k(\alpha)$. In the limit of small values of t , however, a Taylor series expansion yields

$$k(\alpha) = \frac{1}{1 + 32^{1/4} \pi \alpha \bar{\mu} \xi_R} \quad (17)$$

where $\xi_R = R/\lambda_s$ is the dimensionless slenderness of the rod.

Plugging Eq. (17) into Eq. (12) leads to our final result for the extended helical buckling length of a rod that is simultaneously injected and rotated into a cylindrical constraint and that takes into account anisotropic friction effects

$$\bar{l}_h \approx \frac{1}{1 + 32^{1/4} \pi \alpha \xi_R \bar{\mu}} \left([1 + \alpha^2][1 + (1 + \mu_t^2)\alpha^2] \right)^{1/4} \quad (18)$$

A simpler version of this theory can be obtained by neglecting the reduction in the buckling force due to twisting. This is equivalent to setting $k(\alpha) = 1$ in Eq. (12)

$$\bar{l}_h = ([1 + \alpha^2][1 + (1 + \mu_t^2)\alpha^2])^{1/4} \quad (19)$$

which is valid in the limit of $\alpha \bar{\mu} \zeta_r \ll 1$. Physically, this limit corresponds to situations in which the torque along the rod is small, which can be achieved by: (a) lowering the rotational speed such that transverse friction is small (low α), (b) lowering the transverse friction coefficient (low $\bar{\mu}$), or (c) reducing the rod radius since the friction-induced torque is linearly proportional to the rod radius (low ζ_r).

6 Experimental Results, Part II: Validation of Assumptions in the Theory

Prior to comparing the predictions from the theory that was just derived against the experimental results on the extension of reach (this is done in Sec. 7, below), we first perform an experimental validation of the three main underlying assumptions of the theory. First, we show that the twist imposed by the axial rotation at the injector is transported all the way to the tip of the rod. Second, we examine the assumption given by Eq. (10) that the rod rises up to an angle, θ_r , due to the imposed rotation. Third, we confirm that the friction between the rod and the constraint is anisotropic by independently measuring the transverse frictional coefficient, μ_t , and comparing it to the axial frictional coefficient, μ_a , that we measured previously for this setup [27].

6.1 Transport of Twist Along the Rod. To test whether the twist imposed at the rotating injector is transported along the entire length of the rod, we quantified the rotation speed of the tip of the rod, Ω , during injection. This value was then compared to the drive rotation speed, ω ; any differences between Ω and ω due to buildup of twist along the rod would reach a maximum value at its tip. To measure Ω , we marked the surface of the tip of the rod with a small ink spot (≈ 1.5 mm diameter) and imaged it throughout an injection experiment, using a digital camcorder at 120 fps. The resulting videos were postprocessed to estimate $1/\Omega$ from the time required for the ink spot to make one full revolution. These experiments were performed with a constraining pipe of diameter $D = 21.7$ mm, at the injection speed of $v = 1$ cm/s.

In Fig. 4, we plot the measured value of the average tip rotation speed Ω , over a turn, as a function of the normalized injected length, $\bar{l} = l/l_h$, for five values of drive rotation speeds in the range $60 \leq \omega$ (rpm) ≤ 270 . Each data point in this plot represents the average of five measurements of Ω , and the error bars correspond to the standard deviation. For the majority of the parameters explored, we find that $\Omega \approx \omega$. However, for $\omega \geq 240$ rpm and when the injected length nears the onset of helices ($\bar{l} \approx 1$), large fluctuations in Ω become significant. Despite these fluctuations, we would have expected $\Omega = \omega$, but the fact that this is not the case in this region can be attributed to the small sample size ($N = 5$). Visual inspection of the experiments in this regime did indeed indicate that the tip rotation stopped momentarily before resuming at a speed greater than ω , which is indicative of stick-slip behavior. Still, outside this small region of parameter space with unsteady motion, the rotation of the rod was steady throughout with $\Omega \approx \omega$, which validates the assumption that the rotation speed and thus the velocity ratio α given by Eq. (4) of the rod is constant along its length.

6.2 Rise Angle of the Rod Due to Rotation. An important ingredient of the theoretical model developed in Sec. 5 is the fact that an axially rotated rod rises to an angle from the vertical, θ_r , (see inset of Fig. 1), given by Eq. (10). We have performed a series of experiments to quantify θ_r and compare the results with the theoretical predictions. For this purpose, the borosilicate pipe

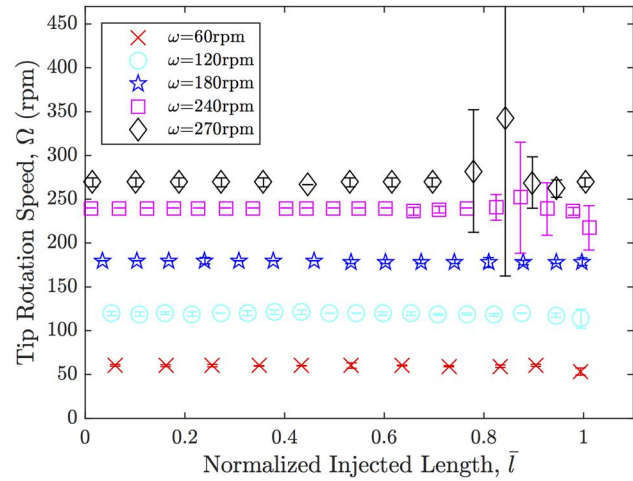


Fig. 4 Rotation speed of the tip, Ω , as a function of the dimensionless injected length $\bar{l} = l/l_h$ (normalized by the helical buckling length l_h), for five different values of the drive rotation speed (see legend). Each data point represents an average of Ω for five full revolutions, and the error bars are the associated standard deviation. The diameter of the cylindrical constraint was $D = 21.7$ mm and the injection speed was $v = 1$ cm/s.

was shortened to 1.21 m, and a rod was injected to $l = 1.20$ m to allow for direct axial visualization within the constraint. Injection was halted, and the rod was then rotated axially at speeds in the range $40 \leq \omega_d$ (rpm) ≤ 300 . During rotation, the apparatus was imaged by a digital camera from the extremity of the constraint, and the videos were processed to track the rod tip and obtain time-series of $\theta_r(t)$.

In Fig. 5(a), we plot a representative time-series of the rise angle (for $\omega = 100$ rpm and $D = 21.7$ mm) which shows that θ_r is not constant as assumed in our theory. Instead, θ_r exhibits highly periodic oscillations about a well-defined average value. This periodic behavior was observed for all values of ω investigated. To extract information on the frequency content of the $\theta_r(t)$ signals, we performed a fast Fourier transform (FFT) for different values of ω and the results are plotted in Fig. 5(b). The drive rotation speed, ω , is plotted on the x-axis; the FFT frequency content, f , is plotted on the y-axis and the FFT amplitude, $A_{\text{FFT}}/A_{\text{max}}$ (normalized by the maximum value at each ω), is given by the gray scale in the adjacent colorbar. The main peak of the FFT occurs along the fundamental frequency $f = \omega$ (solid line), and the other secondary peaks correspond to harmonics of the drive rotation speed represented by the dashed lines (see legend in Fig. 5(b)). If the observed periodicity was due to an intrinsic dynamic behavior of the rod, we would have expected the frequency components of $\theta_r(t)$ to be independent of ω , or if a parametric instability was at play, we would have expected subharmonic behavior, both of which are not the case. As such, we speculate that the periodic behavior of $\theta_r(t)$ can be attributed to small imperfections on the surface finish of the rod during axial rotation.

In Fig. 5(b), we now take the average of the rise angle, $\langle \theta_r \rangle$, plot it as a function of the drive rotation speed, and find that it is approximately independent of ω . However, using an isotropic friction coefficient $\mu = \mu_a = \mu_t = 0.54 \pm 0.11$ (horizontal solid line in Fig. 5(b)) the data are significantly below the prediction of Eq. (10). This discrepancy led us to consider the possibility of an anisotropic frictional response due to the rotation, which motivated the development of the theory presented in Sec. 5 that takes this effect into account. Taking the values for the transverse and axial friction coefficients ($\mu_t = 0.21 \pm 0.01$ and $\mu_a = 0.54 \pm 0.11$, respectively) that were independently measured in Sec. 6.3, below and in Ref. [27], and substituting them into Eq. (18) yields a better theoretical prediction (horizontal dashed line in Fig. 5(b)) that is in excellent agreement with the experimental data. This supports

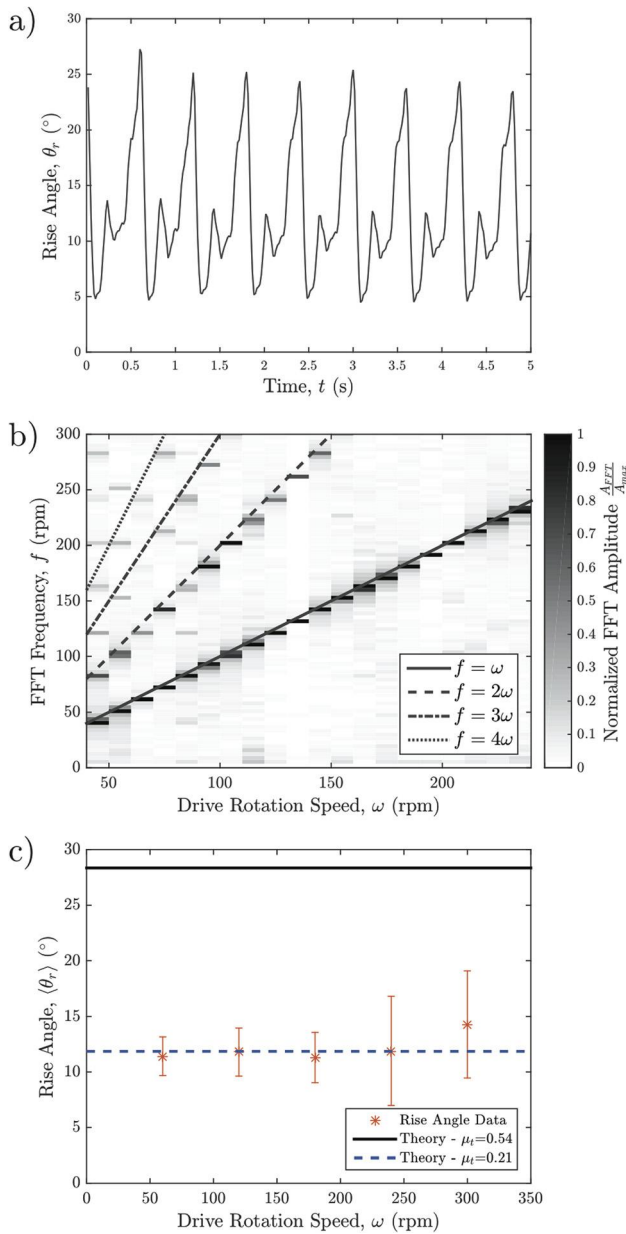


Fig. 5 (a) Typical time-series of rise angle $\theta_r(t)$ for $\omega = 100$ rpm and $D = 21.7$ mm. (b) FFT of the $\theta_r(t)$ signals for different drive rotation speeds. The normalized amplitude of the FFT is provided by the gray scale in the adjacent colorbar. The straight lines correspond to the harmonics of the drive signal (see legend) (c) Average value of the measured rise angle, $\langle \theta_r \rangle$ as a function of drive rotation speed. The horizontal lines represent theoretical prediction for the rise angle based on the measured axial coefficient of friction, $\mu_a = 0.54 \pm 0.05$, (solid line) and the measured tangential frictional coefficient, $\mu_t = 0.21 \pm 0.01$, (dashed line). See Sec. 6.3 on details of how these values were measured.

the anisotropy of the frictional contact during rotation. It remains to experimentally test whether the axial and transverse friction coefficients are indeed different, $\mu_a \neq \mu_t$, and determine their values independently, which is addressed next.

6.3 Axial Versus Transverse Friction Coefficient. The measurements of the average rise angle, $\langle \theta_r \rangle$, described above provided evidence for the anisotropy of friction, given that the isotropic theory from Eq. (10) significantly overpredicted the data (see Fig. 5(c)). In this comparison, we made use of the value

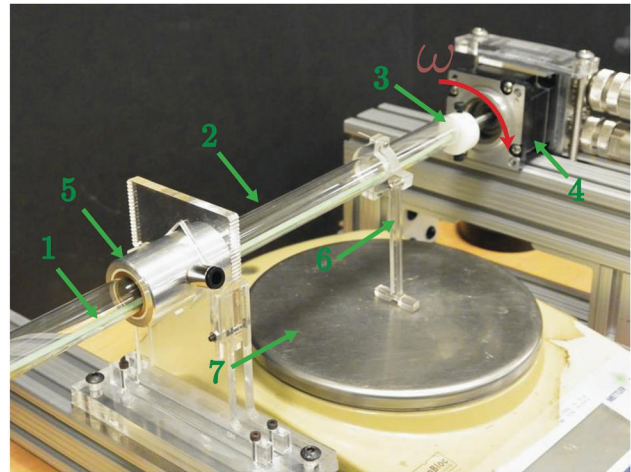


Fig. 6 Apparatus used to measure the transverse friction coefficient, μ_t . A polymeric rod (1) is inserted into a 40 cm length of borosilicate tubing (2) and connected via rod clamp (3) to a servomotor (4) which provides axial rotation. The borosilicate tubing is mounted in a rotary air bushing (5) to allow complete transmission of torque through a tubing-mounted reaction arm (6) to a laboratory scale (7) placed below the apparatus.

$\mu = 0.54 \pm 0.05$ that was previously measured [27] by quantifying the reaction force required to inject a nonrotating rod into a borosilicate constraint (see Ref. [27] for details on these experiments, which included a precision load cell and linear air bearing). This previous protocol yielded the axial friction coefficient, μ_a , and if anisotropic friction is at play, we also need to separately measure the transverse component, μ_t .

In Fig. 6, we present a photograph of the experimental apparatus developed to measure the transverse component of the friction coefficient of the contact between the borosilicate pipe (inner diameter $D = 16.1$ mm and length of 40 cm) and the rotating elastomeric rod. A length of rod was first injected into the pipe in a straight configuration and then rotated at speed ω by clamping one of its extremities to the axis of a servomotor. The constraining pipe was mounted within a rotary air bushing allowing free rotation in the axial direction with negligible rotational friction. A force transmission arm was attached to the outer surface of the pipe to restrict it from rotating, while transmitting all of torque applied by the rod onto a precision laboratory scale (PB3002-S, Mettler Toledo) placed underneath the apparatus.

During an experiment, the rotation of the rod caused it to rise up the cylindrical constraint by an angle θ_r (similarly to the experiments described in Sec. 6.2) and exert a torque on the tubing due to the frictional interaction between the two. The reaction force, F_r , required to resist this torque was measured directly by the laboratory scale with a resolution of $\approx 10^{-4}$ N. The transverse friction coefficient could then be calculated as

$$\mu_t = \frac{2F_r L}{\rho g A \cos(\theta_r) D l_R} \quad (20)$$

where $L = 1.95$ cm is the distance from the center of the tube to the end of the reaction arm; D is the diameter of the pipe; and ρ , A , and l are, respectively, the density, cross-sectional area, and length, of the rod inserted into the constraint. It is important to note that Eq. (20) is independent of ω .

In Fig. 7, we plot the experimental results for the measured transverse friction coefficient, μ_t , as a function of the drive rotation speed, ω , for different values of the length of rod, l , injected into the pipe (see legend). As expected, the data confirm that the transverse friction is independent of ω , as well as of the length of rod. The transverse friction coefficient is therefore a well-defined quantity, with the average value of $\mu_t = 0.21 \pm 0.01$.

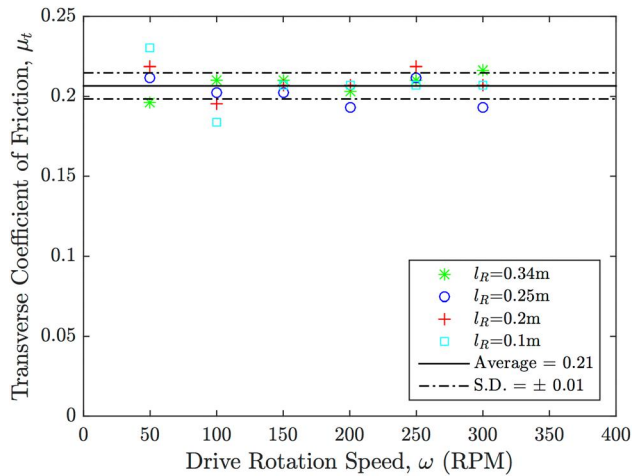


Fig. 7 The transverse friction coefficient, μ_t , is experimentally found to be independent of the rotation speed, ω , and the rod length, l , which is inserted into the constraint. The solid and dashed horizontal lines correspond, respectively, to the average and standard deviation of all the data; $\mu_t = 0.21 \pm 0.01$.

Returning to Fig. 5(c) and plugging this measured value of μ_t into Eq. (10), we obtain a prediction for the rise angle given by the dashed line, which is in excellent agreement with the experimental data. These results confirm that there is a significant anisotropy in friction, which must be taken into account for the theoretical description, as we did in Sec. 5. Whereas the phenomenon is robust, and, if taken into account, yields a predictive description of the experimental data, we have not yet been able to rationalize the underlying physical mechanism for this anisotropy, which should be addressed in a future study. Still, we speculate that the friction anisotropy ($\mu_t \neq \mu_a$) may be due to the specifics of the protocol for the fabrication and surface conditioning of the rod (described in Sec. 3). At the field scale, similar issues of anisotropy may arise on the surface of the wellbore due to the difference in rotation and translation speeds of the string and bit during drilling.

7 Reach Extension: Comparison Between Experiments and Theory

Having developed and validated a theoretical framework to describe how axial rotation of a rod injected into a constraining cylinder can extend the helical buckling length, we finish by performing a direct comparison between the predictions and the experimental data presented in Fig. 3. As expected, the simpler version of the theory that neglects torsional effects, Eq. (19), is not sufficient to accurately describe the full range of experimental results. The version of the theory that assumes anisotropic friction coefficients and takes into account torsional effects, Eq. (18) (solid lines in Fig. 3), provides a significantly better description of the data, especially for larger values of α . It is important to note that Eq. (18) predicts some dependence of the $\bar{l}_h(\alpha)$ curves on the constraint diameter (through the dimensionless slenderness of the rod that depends on the buckling wavelength, which itself depends on the radial clearance of the constraint, Δr). However, this dependence on Δr is not discerned in the experimental data. Still, Eq. (18) provides a satisfactory lower bound for the dependence of \bar{l}_h on α . We highlight that there are no fitting parameters in our theory and that all the required parameters are measured independently.

8 Conclusions

We reported the results from an experiment on the simultaneous injection and continuous axial rotation of an elastic rod into a

horizontal cylindrical constraint with a focus on the extension of reach. Initial experiments demonstrated significant increases in the helical buckling length in the presence of continuous axial rotation of the rod by as much as a factor of approximately 5 within the parameter range explored, when compared to the non-rotating case.

We also presented the results of three experiments designed to verify assumptions made in the derivation of our theory. First, we demonstrated experimentally that the rotation speed of the rod remains constant along its length for the majority of the parameters investigated. Second, we quantified the angle to which the rod rose within the constraint due to axial rotation. The amplitude of this rise angle was found to vary periodically in time instead of the predicted constant level. Moreover, the rise angle was found to be lower than predicted by an initial calculation that assumed isotropic friction. Thus, it was hypothesized that there is anisotropy in the friction coefficient between the rod and the constraint. Finally, we directly measured the value of this friction in the transverse direction. It was found to be significantly lower than that measured previously for the axial direction, confirming the results of our rise angle measurements. Once we accounted for these effects, our theoretical framework showed good agreement with experimental results for the helical buckling length of a rod injected into a constraint under axial rotation.

We hope that these results will motivate future efforts in exploring the effects of axial rotation on the buckling behavior of an elastic rod injected into a cylindrical constraint. This is a problem with practical relevance to several fields, in particular to coiled tubing operations in the oil/gas industry.

References

- [1] Bassett, E. K., Slocum, A. H., Masiakos, P. T., Pryor, H. I., Farokhzad, O. C., and Karp, J. M., 2009, "Design of a Mechanical Clutch-Based Needle-Insertion Device," *Proc. Natl. Acad. Sci. U.S.A.*, **106**(14), pp. 5540–5545.
- [2] Svesšek, D., and Podgornik, R., 2008, "Confined Nanorods: Jamming Due to Helical Buckling," *Phys. Rev. E*, **77**(3), p. 031808.
- [3] Silverberg, J. L., Noar, R. D., Packer, M. S., Harrison, M. J., Henley, C. L., Cohen, I., and Gerbode, S. J., 2012, "3D Imaging and Mechanical Modeling of Helical Buckling in Medicago Truncatula Plant Roots," *Proc. Natl. Acad. Sci. U.S.A.*, **109**(42), pp. 16794–16799.
- [4] Acock, A., ORourke, T., Shirmboh, D., Alexander, J., Andersen, G., Kaneko, T., Venkitaraman, A., Lopez-de Cardenas, J., Nishi, M., Numasawa, M., Yoshioka, K., Roy, A., Wilson, A., and Twynam, A., 2004, "Practical Approaches to Sand Management," *Oilfield Rev.*, **16**(1), pp. 10–27.
- [5] Afghoul, A., Amaravadi, S., Boumali, A., Calmeto, J., Lima, J., Lovell, J., Tinkham, S., Zemlak, K., and Staal, T., 1994, "Coiled Tubing: The Next Generation," *Oilfield Rev.*, **6**(4), pp. 9–23.
- [6] McCourt, L., Truslove, T., and Kubie, J., 2002, "Penetration of Tubulars Into Horizontal Oil Wells," *Proc. Inst. Mech. Eng., Part C*, **216**(12), pp. 1237–1245.
- [7] van Adrichem, W., and Newman, K., 1993, "Validation of Coiled-Tubing Penetration Predictions in Horizontal Wells," *J. Pet. Technol.*, **45**(2), pp. 155–159.
- [8] Bennetzen, B., Fuller, J., Isecan, E., Krepp, T., Meehan, R., Mohammed, N., Poupeau, J. F., and Sonowal, K., 2010, "Extended-Reach Wells," *Oilfield Rev.*, **22**(3), pp. 4–15.
- [9] Summers, T., Larsen, H. A., Redway, M., and Hill, G., 1995, "The Use of Coiled Tubing During the Wytch Farm Extended Reach Drilling Project," *J. Pet. Technol.*, **47**(5), pp. 23–36.
- [10] Lubinski, A., 1950, "A Study of the Buckling of Rotary Drilling Strings," *Drilling and Production Practice Conference*, New York, Jan. 1, Paper No. API-50-178, pp. 178–214.
- [11] Lubinski, A., and Althouse, W., 1962, "Helical Buckling of Tubing Sealed in Packers," *J. Pet. Technol.*, **14**(6), pp. 655–670.
- [12] Cheatham, J. B., Jr., 1984, "Helical Postbuckling Configuration of a Weightless Column Under the Action of Axial Load," *Soc. Pet. Eng. J.*, **24**(4), pp. 467–472.
- [13] Chen, Y., Lin, Y., and Cheatham, J., 1990, "Tubing and Casing Buckling in Horizontal Wells (Includes Associated Papers 21257 and 21308)," *J. Pet. Technol.*, **42**(2), pp. 140–141.
- [14] Mitchell, R., 1986, "Simple Frictional Analysis of Helical Buckling of Tubing," *SPE Drill. Eng.*, **1**(6), pp. 457–465.
- [15] Wu, J., and Juvkam-Wold, H., 1993, "Study of Helical Buckling of Pipes in Horizontal Wells," *SPE Production Operations Symposium*, Oklahoma City, OK, Mar. 21–23, pp. 867–876.
- [16] Gao, G., and Miska, S., 2009, "Effects of Boundary Conditions and Friction on Static Buckling of Pipe in a Horizontal Well," *Soc. Pet. Eng. J.*, **14**(4), pp. 782–796.

- [17] Gao, G., and Miska, S., 2010, "Effects of Friction on Post-Buckling Behavior and Axial Load Transfer in a Horizontal Well," *Soc. Pet. Eng. J.*, **15**(4), pp. 1104–1118.
- [18] Miller, J. T., Su, T., Pabon, J., Wicks, N., Bertoldi, K., and Reis, P. M., 2015, "Buckling of a Thin Elastic Rod Inside a Horizontal Cylindrical Constraint," *Extreme Mech. Lett.*, **3**, pp. 36–44.
- [19] McCourt, I., Truslove, T., and Kubie, J., 2004, "On the Penetration of Tubular Drill Pipes in Horizontal Oil Wells," *Proc. Inst. Mech. Eng., Part C*, **218**(9), pp. 1063–1081.
- [20] Wicks, N., Wardle, B. L., and Pafitis, D., 2008, "Horizontal Cylinder-in-Cylinder Buckling Under Compression and Torsion: Review and Application to Composite Drill Pipe," *Int. J. Mech. Sci.*, **50**(3), pp. 538–549.
- [21] McCourt, I., and Kubie, J., 2005, "Limits on the Penetration of Coiled Tubing in Horizontal Oil Wells: Effect of the Pipe Geometry," *Proc. Inst. Mech. Eng., Part C*, **219**(11), pp. 1191–1197.
- [22] Bhalla, K., 1995, "Coiled Tubing Extended Reach Technology," *Offshore Europe*, Aberdeen, UK, Sept. 5–8, Paper No. SPE-30404-MS.
- [23] Al Shehri, A. M., Al-Driweesh, S. M., Al Omari, M., and Al Sarakbi, S., 2007, "Case Study: Application of Oiled Tubing Tractor to Acid Stimulate Horizontal Extended Reach Open Hole Power Water Injector," *Asia Pacific Oil and Gas Conference and Exhibition*, Jakarta, Indonesia, Oct. 20–Nov. 1, Paper No. SPE-110382-MS.
- [24] Newman, K. R., 2007, "Vibration and Rotation Considerations in Extending Coiled-Tubing Reach," *SPE ICoTA Coiled Tubing and Well Intervention Conference and Exhibition*, The Woodlands, TX, Mar. 20–21, Paper No. SPE-106979-MS.
- [25] Miller, J. T., Mulcahy, C. G., Pabon, J., Wicks, N., and Reis, P. M., 2015, "Extending the Reach of a Rod Injected Into a Cylinder Through Distributed Vibration," *ASME J. Appl. Mech.*, **82**(2), p. 021003.
- [26] Leising, L., Onyia, E., Townsend, S., Paslay, P., and Stein, D., 1997, "Extending the Reach of Coiled Tubing Drilling (Thrusters, Equalizers and Tractors)," *SPE/IADC Drilling Conference*, Amsterdam, Mar. 4–6, Paper No. SPE-37656-MS.
- [27] Miller, J. T., Su, T., Dussan, V. E., Pabon, J., Wicks, N., Bertoldi, K., and Reis, P. M., 2015, "Buckling-Induced Lock-Up of a Slender Rod Injected Into a Horizontal Cylinder," *Int. J. Solids Struct.*, **72**, pp. 153–164.
- [28] Love, A. E. H., 2013, *A Treatise on the Mathematical Theory of Elasticity*, Vol. 1, Cambridge University Press, Cambridge, UK.
- [29] Paslay, P., and Bogy, D., 1964, "The Stability of a Circular Rod Laterally Constrained to be in Contact With an Inclined Circular Cylinder," *ASME J. Appl. Mech.*, **31**(4), pp. 605–610.
- [30] Miska, S., and Cunha, J., 1995, "An Analysis of Helical Buckling of Tubulars Subjected to Axial and Torsional Loading in Inclined Wellbores," *SPE Production Operations Symposium*, Oklahoma City, OK, Apr. 2–4, Paper No. SPE-29460-MS.
- [31] Dawson, R., 1984, "Drill Pipe Buckling in Inclined Holes," *J. Pet. Technol.*, **36**(10), pp. 1–734.